Local Structure and Magnetism of La1–xMxPO4 (M = Sm, 239Pu, 241Am) Explained by Experimental and Computational Analyses

Laura Martel, Md. Ashraful Islam, Karin Popa, Jean-François Vigier, Eric Colineau, Hélène Bolvin, Jean-Christophe Griveau

To cite this version:

Laura Martel, Md. Ashraful Islam, Karin Popa, Jean-François Vigier, Eric Colineau, et al.. Local Structure and Magnetism of La1–xMxPO4 (M = Sm, 239Pu, 241Am) Explained by Experimental and Computational Analyses. Journal of Physical Chemistry C, 2021, 125 (40), pp.22163-22174. 10.1021/acs.jpcc.1c03957 . hal-03414627

THE JOURNAL OF PHYSICAL CHEMISTRY C
A JOURNAL OF THE AMERICAN CHEMICAL SOCIETY

pubs.acs.org/JPCC

Article

Local Structure and Magnetism of $La_{1-x}M_xPO_4$ (M = Sm, ^{239}Pu, ^{241}Am) Explained by Experimental and Computational Analyses

Laura Martel,* Md. Ashraful Islam, Karin Popa, Jean-Francois Vigier, Eric Colineau, Hélène Bolvin, and Jean-Christophe Griveau*

Cite This: *J. Phys. Chem. C* 2021, 125, 22163−22174

Read Online

ACCESS | Metrics & More | Article Recommendations | Supporting Information

ABSTRACT: With their high chemical and self-irradiation stability, crystalline monazites are among the most promising materials for the encapsulation of nuclear wastes. Yet, the local and magnetic structures of the matrices doped with low-content actinide cation, depicted as most resistant, are still unclear. This limits the development of theoretical approaches predicting their behavior under extreme conditions—self-irradiation and long-term leaching. Here, we characterize the model matrices $La_{1-x}M_xPO_4$ ($0 \leq x \leq 0.10$)—with M = Sm, ^{239}Pu, ^{241}Am—by X-ray diffraction and solid-state ^{31}P NMR. As an example, we confirm that $La_{0.96}{}^{241}Am_{0.04}PO_4$ has higher self-irradiation resistance compared to $^{241}AmPO_4$. Further, computational analyses show that magnetic properties of the Pu complex are strongly affected by the *J*-mixing and the paramagnetic NMR shifts are dominated by the Fermi contact contribution, arising from delocalization of the spin density of the cation toward the phosphorus through the bonds.

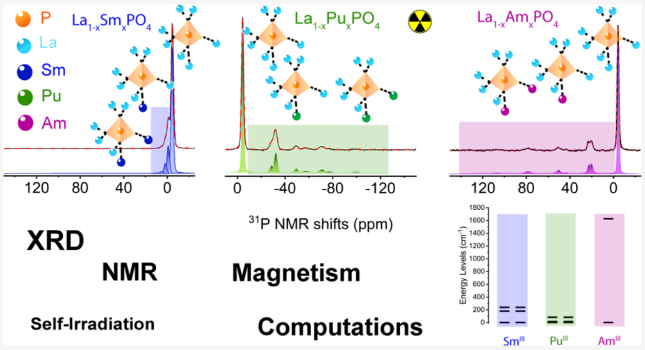

1. INTRODUCTION

In most countries, the lead directives for managing nuclear wastes are through deep geological disposal in glasses, metals, and crystalline ceramics.[1] Among the ceramics, the physical and chemical durability of phosphate monazites is proven by the discovery of a well-crystallized 2-billion-year-old sample;[2] their low alteration to leaching;[3] and their high self-healing capacity as the α-decay produced is sufficient to repair the structure damaged by the recoil nuclei.[4] The optimal actinide content inserted into the $LaPO_4$-doped matrices was determined to be under 10 wt %.[5] To develop models predicting the effects under self- or external irradiation, strong experimental data are necessary. Unfortunately, while the long-range structure is probed by X-ray diffraction (XRD), due to the low actinide content, the understanding of the atomic scale structure remains unknown. Indeed, results on a series of $La_{1-x}Pu_xPO_4$ using Pu-L_{III} extended X-ray absorption fine structure (EXAFS) and X-ray absorption near-edge spectroscopy (XANES) shows unclear outputs as the spectra were similar.[6] Magic angle spinning (MAS)-NMR is a good alternative for such atomic scale analyses as it is sensitive to order, disorder,[7] and probing low metal content.[8−10] With the unpaired 5f electrons, MAS-NMR has also a powerful dual capability: structural and magnetic. Improving the understanding of magnetism and NMR spectra combined with computational studies is booming, due to their technological impact in the analytical characterization of materials[11] and organometallics.[12] In this work, we successfully explain the atomic scale structure and magnetism of $La_{1-x}M_xPO_4$ ($0 \leq x \leq 0.10$)—with M = Sm, ^{239}Pu, ^{241}Am—nuclear wastes matrices based on computational analyses.

2. METHODS

2.1. Sample Preparation. Caution! ^{239}Pu ($t_{1/2}$ = 24 110 years), ^{241}Am ($t_{1/2}$ = 432 years) and its daughters have high specific activity α-particle and γ emitting radionuclides, and their use presents extreme hazards to human health. This research was conducted in radiological and nuclear facilities with safe handling and manipulation of these radiotoxic materials.

The $La_{1-x}Sm_xPO_4$ solid solution (x = 0.01, 0.05, 0.10, and 0.15) was prepared by sol−gel reaction using a procedure modified from Geisler et al.[13] Stoichiometric amounts of La_2O_3 (Alfa Aesar, 99.99%) and Sm_2O_3 (Merck, 99.99%) were dissolved in HNO_3 (Merck, 63%). An excess of H_3PO_4 (Merck, 85%) ($(Sm^{3+} + La^{3+})/PO_4{}^{3-}$ = 1:1.1) was added dropwise under continuous heating (343.15 K) and stirring; this initiated the precipitation of a white gel. After 1 h, ammonium hydroxide solution (Merck, 25%) was added till pH = 5. The

Received: May 3, 2021
Revised: August 14, 2021
Published: October 5, 2021

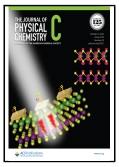

ACS Publications

https://doi.org/10.1021/acs.jpcc.1c03957
J. Phys. Chem. C 2021, 125, 22163−22174

Table 1. XRD Parameters for $La_xM_{1-x}PO_4$ (M = Sm, Pu, and Am)

name	dose (α g^{-1} day^{-1})	a	b	c	α, γ	β	V
$La_{0.99}Sm_{0.01}PO_4$	0	6.837449	7.073059	6.508413	90	103.2926	306.32
$La_{0.95}Sm_{0.05}PO_4$	0	6.832399	7.067482	6.503616	90	103.3112	305.61
$La_{0.90}Sm_{0.10}PO_4$	0	6.825891	7.058657	6.498964	90	103.3446	304.68
$AmPO_4$	0	6.753	6.967	6.433	90	103.787	293.9351
$La_{0.96}Am_{0.04}PO_4$	0	6.83766	7.070373	6.510631	90	103.3074	306.3038
	8.80495×10^{16}	6.84097	7.07343	6.51545	90	103.3352	306.77657
	1.1882×10^{17}	6.84139	7.07394	6.51637	90	103.3387	306.85563

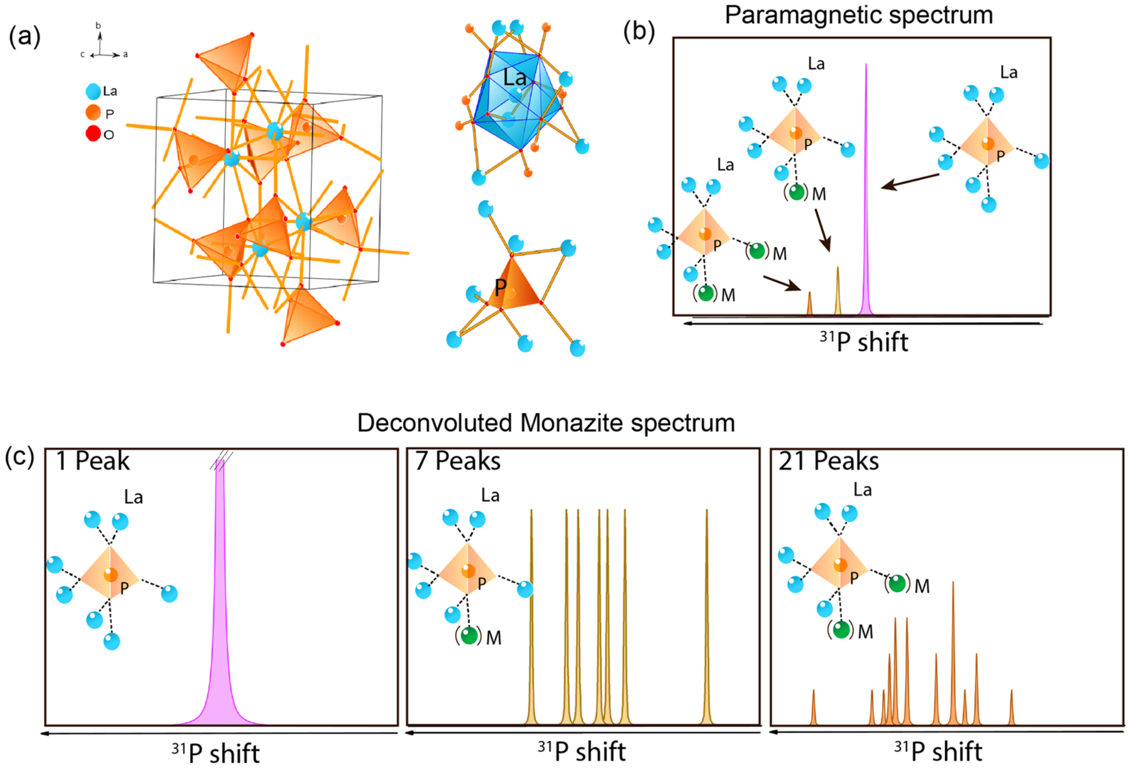

Figure 1. Monazite crystalline structure with $LaPO_4$ set as an example for the series (a). Schematic ^{31}P MAS-NMR spectrum in the specific case of the low-content paramagnetic cation M^{3+} for which three $P(OLa)_y(OM)_{1-y}$ species are expected considering a randomly distributed network (RDN). The ^{31}P signal of each species is expressed due to a magnetic inequivalency (b), and for the monazites, to a magnetic and spatial inequivalency (c).

precipitates were separated from solution by centrifugation and washed several times with water. After drying in air, the powders were calcined for 10 h under air in alumina crucibles at 1673.15 K. The $La_{1-x}Am_xPO_4$ solid solution was prepared by solid-state reaction, as in the case of their Pu-containing counterparts (see ref 6). La_2O_3 (Aldrich, 99.99%), $^{241}AmO_2$ (containing about 7% ^{237}Np and 2% ^{239}Pu), and $(NH_4)_2HPO_4$ (Aldrich, 99.99%) were used as starting reagents without further purification. La_2O_3 and AmO_2 in corresponding stoichiometric ratios and $(NH_4)_2HPO_4$ were mixed and ground in an agate mortar and pressed into disks. The disks were fired slowly (heating and cooling ramps of 200 °C h^{-1}) under an argon atmosphere (purity: 99.96%, containing less than 7 ppm H_2O): for $La_{0.96}Am_{0.04}PO_4$ composition, 6 h at 1473.15 K.

2.2. X-ray Diffraction. All samples were characterized by powder XRD using a dedicated Bruker D8 Advance diffractometer (Cu Kα radiation, 40 kV, and 40 mA), embedded in a radioactive glovebox, with a Bragg−Brentano $\theta/2\theta$ configuration and equipped with a curved Ge monochromator (1,1,1) and a Lynxeye linear position-sensitive detector. The powder patterns were recorded using a step size of 0.0197° across the angular range of $10° \leq 2\theta \leq 120°$ on about 15−20 mg of a prepared powder sample. The actinide-based monazite powders were loaded in an epoxy resin to fix them and prevent their dispersion.

2.3. ^{31}P MAS-NMR. All experiments were performed on a Bruker AVANCE III 9.4 T spectrometer with an NMR probe embedded in a nuclear glovebox.[14] The spectra were recorded at 50 kHz at a ^{31}P Larmor frequency of 161.976 MHz. Single-pulse experiments were done using a 90° pulse length of 3 μs, and the recycling delays were adjusted between ∼1500 and 1 s to record quantitative spectra.

2.4. Magnetic Susceptibility Measurements. They were recorded using a magnetic property measurement system (MPMS—Quantum Design) in the temperature range of 2−300 K in applied magnetic fields between 0.5 and 7 T. All radioactive samples were manipulated following the corresponding regulations.

2.5. Ab Initio Calculations. Calculations were performed using MOLCAS-7.8[15] suite of software on the clusters $[MLa_9(PO_4)_7]^{9+}$ (M = Sm^{3+}, Pu^{3+}, Am^{3+}) based on the XRD structure of $LaPO_4$.[16] The substitution of a La^{3+} cation by either Sm^{3+} or Pu^{3+} without deforming the coordination sphere was

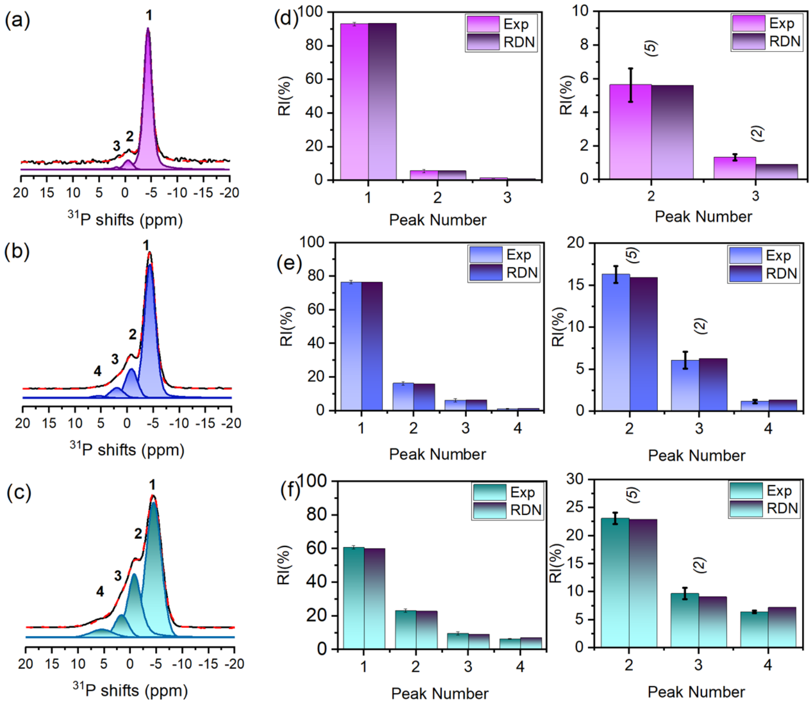

Figure 2. ^{31}P MAS-NMR spectra of $La_{0.99}Sm_{0.01}PO_4$ (a), $La_{0.95}Sm_{0.05}PO_4$ (b), and $La_{0.90}Sm_{0.10}PO_4$ (c). The chart boxes correspond to the experimental and theoretical (RDN) relative intensities of each peak for (d) $La_{0.99}Sm_{0.01}PO_4$, (e) $La_{0.95}Sm_{0.05}PO_4$, and (f) $La_{0.90}Sm_{0.10}PO_4$. For clarity, we enlarged each chart box for the low relative intensities on the right-hand side. The numbers in parentheses correspond to the number of peaks overlapping.

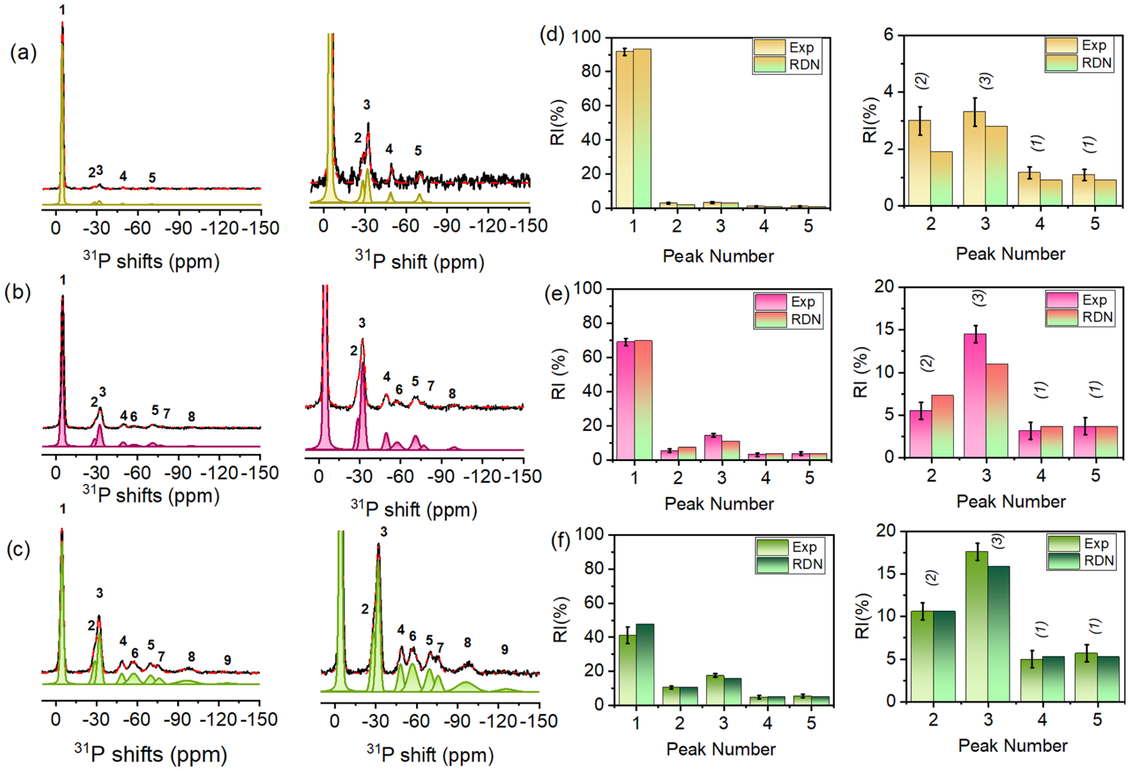

Figure 3. ^{31}P MAS-NMR spectra of (a) $La_{0.99}Pu_{0.01}PO_4$, (b) $La_{0.95}Pu_{0.05}PO_4$, and (c) $La_{0.90}Pu_{0.10}PO_4$. The chart boxes correspond to the experimental and RDN relative intensities of each peak for (d) $La_{0.99}Pu_{0.01}PO_4$, (e) $La_{0.95}Pu_{0.05}PO_4$, and (f) $La_{0.90}Pu_{0.10}PO_4$. For clarity, we enlarged each spectrum and chart box for the low relative intensities on the right-hand side. Also, we only presented the RDN for peaks that could be properly differentiated. The numbers in parentheses correspond to the number of peaks overlapping.

justified by the close ionic radii for the La, Sm, and Pu trivalent ions (1.17, 1.10, and 1.14 Å, respectively). Since the substituted cations are more contracted than the cations of the host crystal, one can expect the deformation to be negligible. This cluster

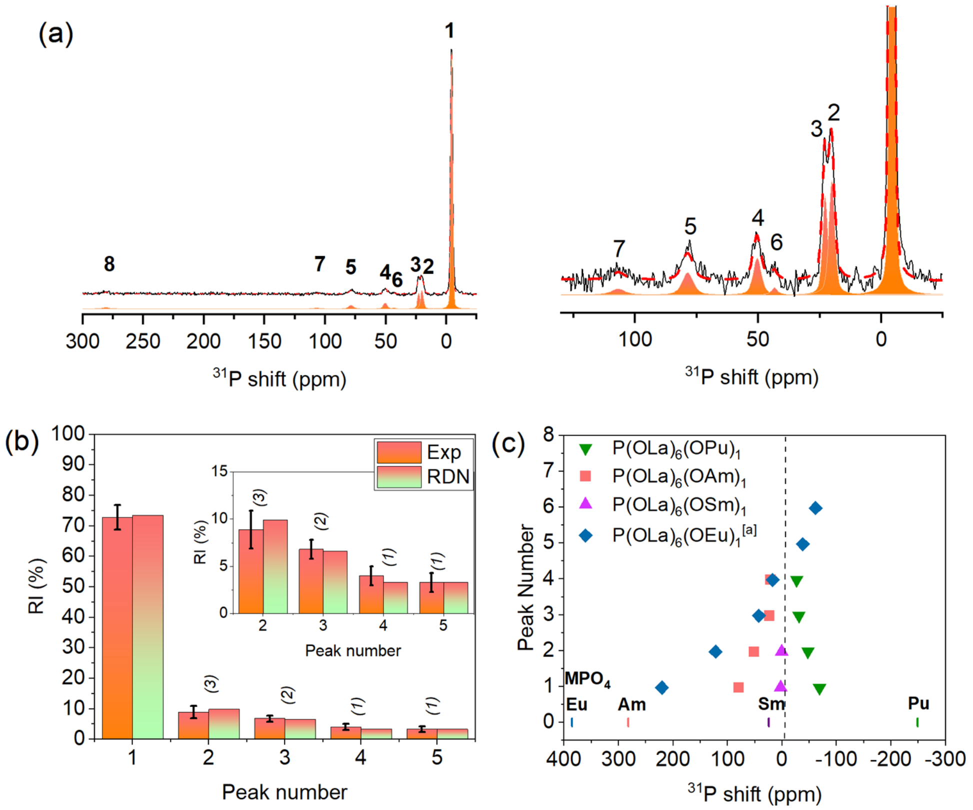

Figure 4. (a) ^{31}P MAS-NMR spectrum of $La_{0.96}Am_{0.04}PO_4$. On the right is presented an enlargement of the spectrum showing the low-intensity peaks. (b) Experimental and RDN relative intensities (an enlargement of the low relative intensities is shown in the inset). The numbers in parentheses correspond to the number of peaks overlapping. (c) Summary of the paramagnetic shifts of $P(OLa)_6(OM)_1$ units obtained for the composition $La_{0.90}Am_{0.10}PO_4$ (the values for Eu are from ref 9).

consists of the central M^{3+} cation and the nine next nearest-neighbor La^{3+} cations completed with the neighboring PO_4 polyhedra. This cluster was further embedded in a sphere of point charges of radius 20 Å. The charges were deduced using LoProp charge analysis[17] after a Hartree−Fock (HF) calculation on $[La_{10}(PO_4)_7]^{9+}$ with ANO-RCC-DZP basis: +2.4, +2.0, and −1.1 for La, P, and O, respectively. Then, spin−orbit complete active space self-consistent field (SO-CASSCF) calculations were performed using relativistically contracted ANO-RCC basis sets,[18] QZP for Pu or Sm and TZP for P and O; the ECP-LanL2DZ pseudopotential and the corresponding basis set was used for La atoms.[19] First, spin-free complete active space self-consistent field (SF-CASSCF)[20] calculations were performed with an active space of seven f orbitals (for Sm 4f and for Pu 5f) and associated electrons, i.e., CAS (n,7). Douglas−Kroll−Hess transformed Hamiltonian (DKH2) was used to treat the relativistic effects.[21,22] Spin−orbit coupling was calculated as a state interaction between the SF-CASSCF states with the restricted active space state interaction (RASSI) code.[23] Spin−orbit integrals were calculated using atomic mean field integrals (AMFI) approximation.[24] g-Values were calculated according to ref 25, and crystal field parameters (CFPs) were deduced with a local program written in Mathematica as described in refs 26 and 27.

3. RESULTS AND DISCUSSION

3.1. Long Range and Local Structure of $La_{1-x}M_xPO_4$ Monazites.

We synthesized the matrices $La_{1-x}Sm_xPO_4$ (x = 0.01, 0.05, and 0.10), $La_{1-x}Pu_xPO_4$ (x = 0.01, 0.05, and 0.10), and $La_{1-x}Am_xPO_4$ (x = 0.04). The rare earth is the electronic counterpart to the actinide—$La_{1-x}Eu_xPO_4$ was published in ref 9. They were characterized by XRD and ^{31}P MAS-NMR. The XRD pattern analyses underline that they are single-phased (except for $La_{0.96}Am_{0.04}PO_4$ which has ∼3% of $AmPO_4$) and that the lattice volumes (bond length and angles) in the solid solutions decrease with increasing M content (Table 1, Figure S1, and ref 6). They crystallize in the monazite ($P2_1/n$) space group; this structure has one M site with a coordination number of nine and one P site linked as a tetrahedron to four inequivalent O sites (Figure 1a).

The second analytical technique, MAS-NMR, has the unique dual ability to probe the atomic scale and to be sensitive to the cation—M—magnetism. Indeed, for a diamagnetic compound, one crystallographic site corresponds to one NMR peak. In the simplest case—a randomly distributed network (RDN) and a metal content under ∼10 mol %—adding one paramagnetic cation to the diamagnetic matrix leads to an NMR spectrum with three signals of the P sites surrounded by: seven La, six La, one M, and five La and two M (Figure 1b). They are denoted $P(OLa)_m(OM)_{7-m}$ units (m = 7, 6, 5). Now, for the monazite structure case,[8,9] each $P(OLa)_m(OM)_{7-m}$ unit ($m < 7$) becomes inequivalent also with the cation spatial position. Thus, the ^{31}P MAS-NMR spectrum presents (Figure 1c) a main peak for the $P(OLa)_7$ unit; seven peaks, with the same relative intensities (RI), for the $P(OLa)_6(OM)_1$ units; and 21 peaks, with the same RI, for the $P(OLa)_5(OM)_2$ units. (The reader can find the exact formula and more details in ref 9.) The NMR shift for the $P(OLa)_7$ unit is called $\delta_{dia} = \delta_{LaPO_4}$ as it is the spectral signature of P atoms only surrounded by diamagnetic cations and its value is equal to $LaPO_4$ chemical shift.

Table 2. Experimental ^{31}P NMR Shifts, δ_{exp}, for $La_{1-x}M_xPO_4$ (M = Sm, Pu, Am); the Uncertainties Are of ±0.2 ppm

	$La_{1-x}Sm_xPO_4$				$La_{1-x}Pu_xPO_4$				$La_{1-x}Am_xPO_4$
peak no.	$x = 0.01$	$x = 0.05$	$x = 0.10$	peak no.	$x = 0.01$	$x = 0.05$	$x = 0.10$	peak no.	$x = 0.04$
1	−4.3	−4.5	−4.5	1	−4.5	−4.7	−4.6	1	−4.5
2	−0.6	−0.8	−0.8	2	−27.9	−28.5	−28.9	2	22.8
3	1.7	1.7	1.7	3	−31.8	−31.9	−32.2	3	20.1
4		5.5	5.5	4	−48.7	−48.8	−48.6	4	50.4
				5	−69.8	−69.9	−69.9	5	78.6
				6		−57.0	−57.4	6	43.4
				7		−75.9	−76.2	7	106.9
				8		−97.1	−96.6	8	280.9
				9			−126.3		

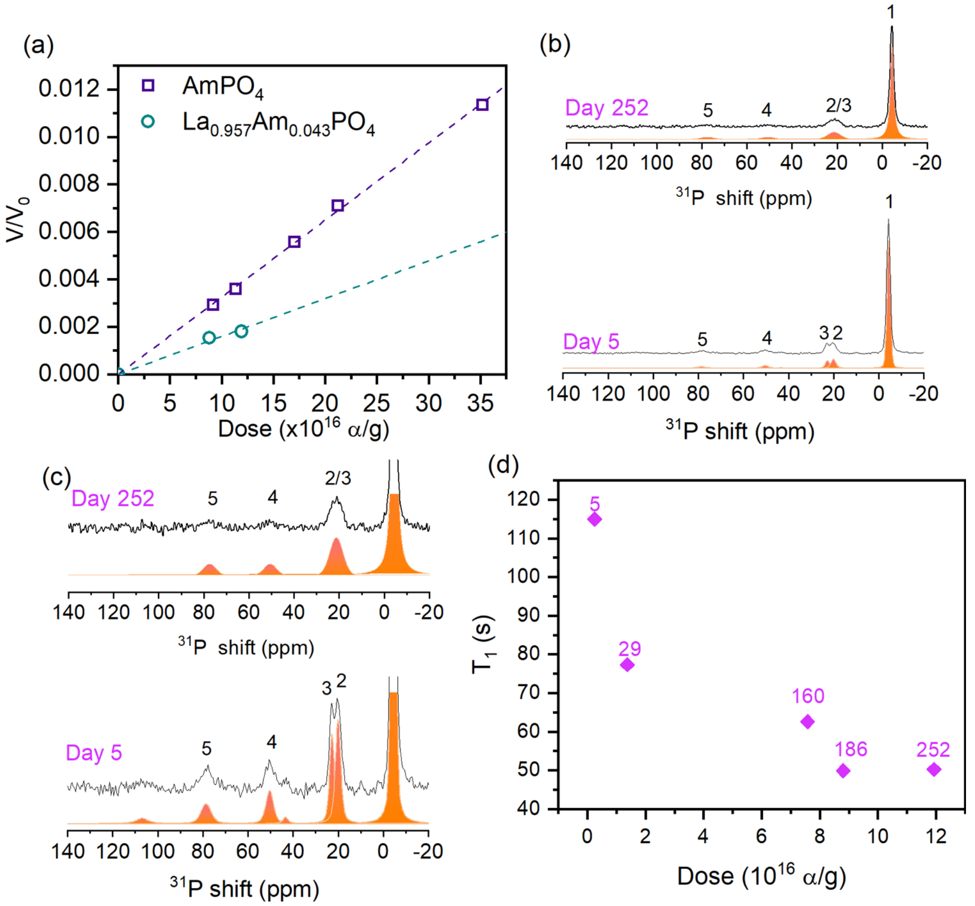

Figure 5. $La_{0.96}Am_{0.04}PO_4$. (a) Variation under self-irradiation damage of the relative lattice variation (V/V_0) extracted from XRD. The dashed lines are the corresponding linear fits. (b) Self-irradiation damage observed by ^{31}P MAS-NMR spectra and (c) enlarged ^{31}P MAS-NMR spectra on the low-intensity peaks. (d) Spin−lattice relaxation time (T_1) of the $P(Ola)_7$ units (the purple numbers correspond to the number of days).

Figures 2 and 3 show—respectively—the experimental ^{31}P MAS-NMR spectra of $La_{1-x}Sm_xPO_4$ and $La_{1-x}Pu_xPO_4$ with the same M electronic configuration nf^5 ($n = 4$ or 5). We compared their experimental and theoretical relative intensities in the plot charts. For $La_{1-x}Sm_xPO_4$ ($0 < x < 1$), the MAS-NMR spectra were published,[28] but, the authors neither reported nor discussed the $P(OLa)_m(OM)_{7-m}$ units. We can see that each unit is properly identified, and experiment agrees with RDN (Figure 2 and Table S1). For $La_{1-x}Pu_xPO_4$, the $P(OLa)_7$ (peak 1) and $P(OLa)_6(OM)_1$ (peaks 2−5) species present the main experimental relative intensities and can be properly defined—good agreement between RDN and experiment (Figure 3 and Table S2). As the signal of the $P(OLa)_5(OM)_2$ units are overlapping ($La_{1-x}M_xPO_4$ with $x \neq 0.01$), we did not attribute them. Our analyses lead to the following metal contents: $La_{0.988}Pu_{0.012}PO_4$, $La_{0.947}Pu_{0.053}PO_4$, $La_{0.88}Pu_{0.12}PO_4$, $La_{0.99}Sm_{0.01}PO_4$, $La_{0.962}Sm_{0.038}PO_4$, and $La_{0.922}Sm_{0.078}PO_4$. These values strengthen the XRD data. Finally, we recorded the spectrum of $La_{0.96}Am_{0.04}PO_4$ (Figure 4a,b and Table S3) and determined a composition of $La_{0.957}Am_{0.043}PO_4$ (the uncertainty is 0.043 ± 0.008). Peak 8 corresponds to $AmPO_4$[29] with an amount of 2% in agreement with the XRD results. All of the experimental shifts are reported in Table 2. It is worth mentioning that while we can properly identify the $P(OLa)_6(OM)_1$ species, the experimental attribution of each P site based on their crystalline position can unfortunately not be done due to the low signal recorded.

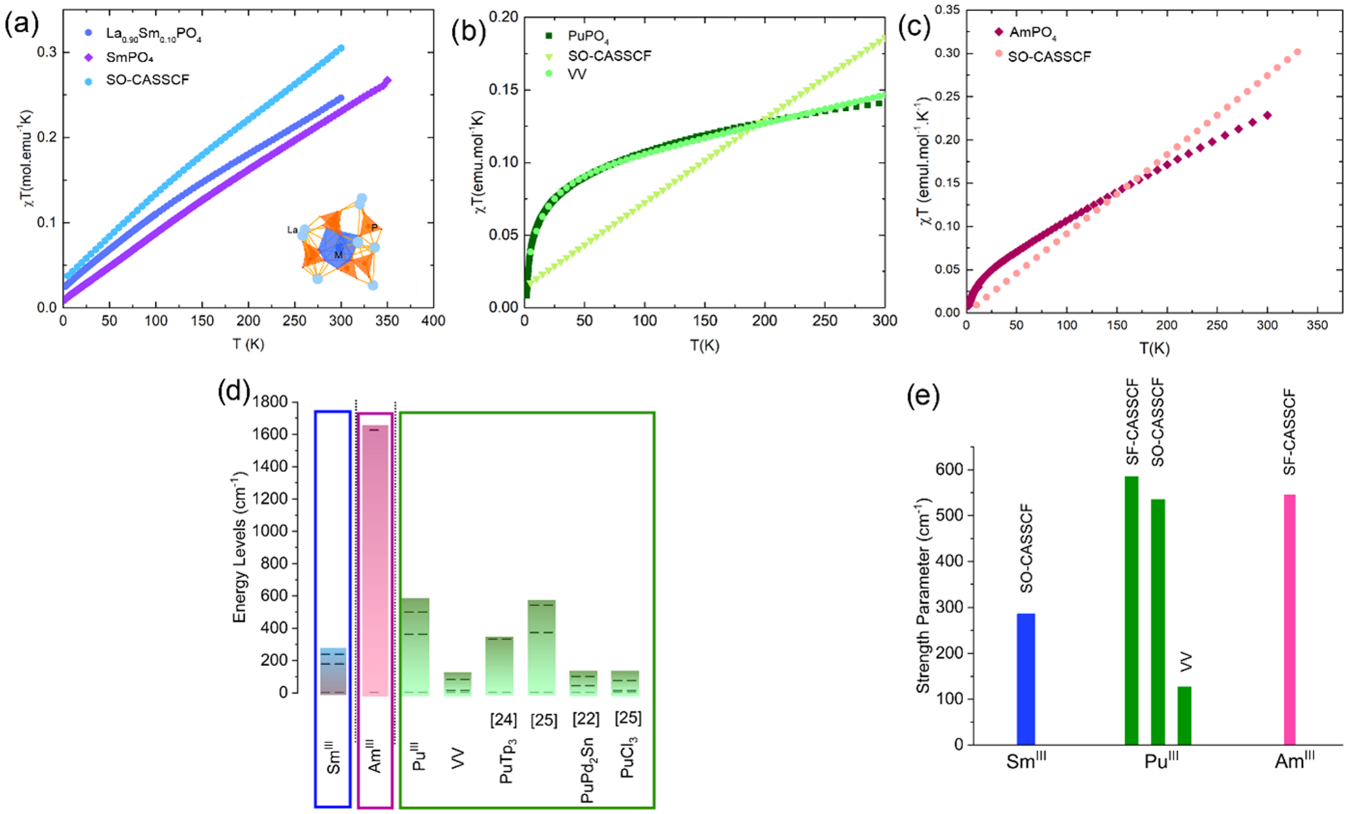

Figure 6. Experimental and computed magnetic susceptibilities of $La_{1-x}Sm_xPO_4$ (x = 0.01 and 1) (a), $PuPO_4$ (b), and $AmPO_4$ (c). (d) Energy levels $^6H_{5/2}$ for Pu and Sm compounds and $^7F_0$ and $^7F_1$ for Am compounds. They are determined in the present study using SO-CASSCF for Sm^{III}, Am^{III}, Pu^{III}, and a Van Vleck (VV) fit (all of the energy levels are available in Table S6). The energy levels were compared with the literature: $PuTp_3$ from Magnani et al.[49] and Gaggioli and Gagliardi,[50] $PuPd_2Sn$[42] and $PuCl_3$.[4343] (e) Total strength parameter S calculated for the M^{III} clusters.

3.2. Self-Irradiation Damages in $La_{0.96}Am_{0.04}PO_4$.

We continued to characterize this sample up to 8 months. XRD shows that the relative lattice variation is, as expected, increasing over time due to lattice swelling and creation of defects (Figure 5a and Table 1). The linear fit used for V/V_0 is an empirical approximation for low doses—with no specific model—allowing us to compare straightforwardly $AmPO_4$ and $La_{0.96}Am_{0.04}PO_4$. A different kind of variation can be expected when the material reaches higher doses and the well-described models[30] cannot be applied for these low doses. Overall, the V/V_0 parameters of $AmPO_4$[29] are almost twice that of $La_{0.96}Am_{0.04}PO_4$ for the same dose (Figure 5a). The present sample is thus more resistant to radiation damage. As the long-range order is lost for $AmPO_4$ for a dose of 4×10^{18} α g^{-1}, about 23 years will be necessary for $La_{0.96}Am_{0.04}PO_4$. The ^{31}P MAS-NMR spectra recorded with self-irradiation damages are presented in Figure 5b,c. After 252 days, there is an overall broadening of the peaks that is more visible for peaks 2 and 3—now overlapping. The creation of defects is indirectly observed as the spin−lattice relaxation time (T_1) of the $P(Ola)_7$ units decreases over time (Figure 5d). Our study could be extended to understand more complex and resistant matrices such as $La_{0.73}{}^{238}Pu_{0.09}Ca_{0.09}Th_{0.09}PO_4$; crystalline for a dose of 7.5×10^{18} α g^{-1}, while $^{238}PuPO_4$ is amorphous—by XRD—at 5×10^{17} α g^{-1}.[31]

3.3. NMR Paramagnetic Shifts.

While NMR is efficient to quantitatively identify the $P(OLa)_m(OM)_{7-m}$ units and characterize these low-metal-content nuclear waste matrices, the analysis of NMR spectra is unfinished without the understanding of the paramagnetic shifts. Indeed, while the ^{31}P NMR shifts of the $P(OLa)_6(OM)_1$ units (peaks 2−5) do not vary with composition (i.e., bond angle or length, Table 1), they are dictated by the M cation magnetism as shown in Figures 4c and S2. The paramagnetic shifts can be determined experimentally using the formula $\delta_{p,exp} = \delta_{exp} - \delta_{dia}$. All of the experimental paramagnetic shifts, $\delta_{p,exp}$, are listed in Table S4. They are in the range of 3−10 ppm for Sm^{III}, −23 to −92 ppm for Pu^{III}, and 27−285 ppm for Am^{III}. The classical model to theoretically calculate the paramagnetic shifts is by summing the Fermi contact (FCS) and the pseudocontact shifts (PCS): $\delta_{p,theo} = \delta_{PCS} + \delta_{FCS}$.[32,33] The former arises from the delocalization of the spin density of the paramagnetic cation toward the P nucleus through the bonds (eq S1), and the latter arises from the through-space dipolar interaction between the electronic magnetic moment of the magnetic center and the nuclear magnetic moment of the nucleus (eqs S2−S5).[34−37] To determine and discuss the two contributions independently based on the components of the magnetic susceptibility tensors, we delved into the magnetism of each sample combining experimental magnetic susceptibility and computational calculations.

3.4. Magnetic Properties.

In a first part, it is important to understand the magnetism of each sample based on experimental results. We recorded magnetic susceptibility curves for $La_{1-x}Sm_xPO_4$ (x = 0.10 and 1), $La_{1-x}Pu_xPO_4$ (x = 0.10 and 1), and $AmPO_4$. The results are depicted in Figure 6 (Note S3 and Figures S3 and S4). We did not analyze $La_{0.96}Am_{0.04}PO_4$ because its contribution will overlap with that of $AmPO_4$. For $La_{1-x}Sm_xPO_4$ (Figure 6a), the curves were fitted with a modified Curie−Weiss $\chi = C/(T - \theta_p) + \chi_0$ (for x = 0.10:

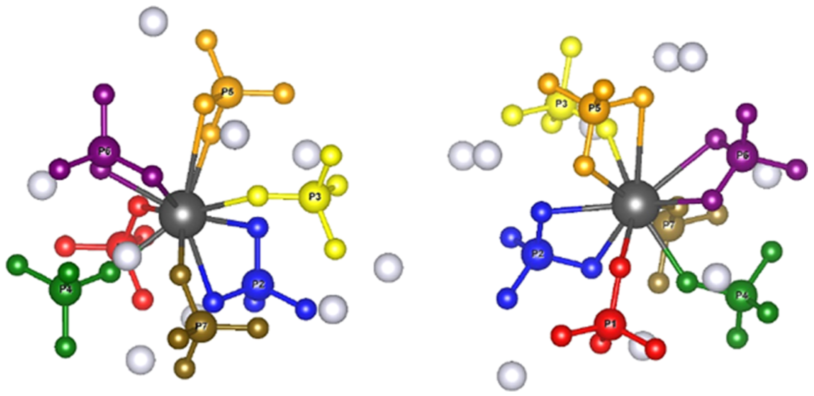

Figure 7. Numbering of the different phosphate groups. Monodentate: P1 (red), P3 (yellow), P4 (green), P7 (brown). Bidentate: P2 (blue), P5 (orange), P6 (purple). Two orientations are proposed.

Table 3. Components of the Magnetic Susceptibility Tensor (in 10^{-3} cm^3 mol^{-1}) from SO-CASSCF for the $[AnLa_9(PO_4)_7]^{9+}$ Complexes at 309 K[a]

An^{III}	J	χ_x^L	χ_x^S	χ_x	χ_y^L	χ_y^S	χ_y	χ_z^L	χ_z^S	χ_z	χ_{iso}
Sm^{III}	all	0.77	0.19	1.15	0.80	0.16	1.12	1.41	−0.32	0.78	1.01
	5/2−7/2	0.77	0.19	1.14	0.81	0.15	1.11	1.43	−0.33	0.77	
	5/2	1.44	−0.55	0.33	1.45	−0.58	0.30	1.86	−0.82	0.23	
Pu^{III}	all	1.37	−0.36	0.64	1.33	−0.35	0.62	1.21	−0.37	0.47	0.58
	5/2−7/2	1.38	−0.37	0.64	1.33	−0.36	0.61	1.22	0.37	1.97	
	5/2	1.61	−0.62	0.36	1.56	−0.61	0.34	1.43	−0.59	0.24	
Am^{III}	all	−1.23	1.17	1.12	−0.72	0.79	0.87	−0.81	0.83	0.85	0.95
	0−1	−1.15	1.17	1.19	−0.77	0.79	0.81	−0.80	0.83	0.85	

[a] L and S denote the orbit and spin contributions. Different spaces for spin−orbit interaction were considered. For the Pu^{III} complex, fitted energy levels are used.

$C = 0.034$, $\theta_p = -2.86$ K, $\chi_0 = 7.3 \times 10^{-4}$ emu mol^{-1}; for $x = 1$: $C = 0.046$, $\theta_p = -0.3$ K, $\chi_0 = 8.8 \times 10^{-4}$ emu mol^{-1}). The presence of the χ_0 term translates the temperature-independent susceptibility, arising due to the diamagnetic and Van Vleck (VV) contributions. For $La_{0.90}Pu_{0.10}PO_4$, while both XRD and NMR confirm a solid solution, an unexpected ferromagnetic impurity was detected (Figure S3). Also, there was no magnetic transition contrary to the previous results reported.[38] This is not surprising as the two compounds differ in volume cell (V = 304.722 Å in the present sample against V = 306.38 Å).[6] For $PuPO_4$, the curve (Figure 6b) was fitted at high temperatures using a modified Curie−Weiss law $\chi = \chi_0 + C/(T - \theta_p)$ (C = 0.097 emu mol^{-1} K, $\chi_0 = 1.3 \times 10^{-4}$ emu mol^{-1}, $\theta_p = -12$ K) and there is a clear antiferromagnetic transition at 4 K. Finally, $AmPO_4$ (Figure 6c) presents a temperature-independent paramagnetism (TIP) curve, χ_{TIP} = 5 emu mol^{-1}, with a low-temperature upturn—reported in numerous ^{241}Am-based materials but having an unclear nature.[39] The deduced experimental effective moment values are: 1.36 μ_B for $SmPO_4$ (T = 300 K), 1.40 μ_B for $La_{0.90}Sm_{0.10}PO_4$ (T = 300 K), and 0.88 μ_B for $PuPO_4$; they agree with the free-ion values of 1.55 μ_B[40] for Sm^{3+} (T = 300 K) and 0.85 μ_B for Pu^{3+}.[4242] This reflects the localized nature of the f-electrons.

In a second part, we used model clusters $[MLa_9(PO_4)_7]^{9+}$ (M = Sm^{3+}, Pu^{3+}, Am^{3+}, named M^{III} later) embedded in a sphere of point charge[41]—shown in Figure 7—to determine the energy levels based on first-principles spin-free (SF)-CASSCF (equivalent to the LS coupling scheme), spin−orbit (SO) complete active space self-consistent field (SO-CASSCF), and spin−orbit complete active space perturbation theory at second-order (SO-CASPT2) calculations. Tables S5 and S6 show all of the computed energy levels. The energy levels for the ground state J = 5/2 manifold ($^6H_{5/2}$) for Sm^{III} and Pu^{III} and, the J = 0 ($^7F_0$) and ($^7F_1$) manifolds for Am^{III} from SO-CASSCF are shown in Figure 6d. For Sm^{III} and Am^{III}, the magnetic susceptibility curves deduced from the ab initio calculations reproduce well the experimental data (Figure 6a,c). For Pu^{III}, the ab initio curves did not agree with the experimental ones (Figure 6b). Using a $[PuCl_6]^{3-}$ complex, we observed that the splitting of the ground $^6H_{5/2}$ term is extremely sensitive to the quartets and to dynamical correlation and a large number of quartet states is necessary. While the SO-CASSCF reduced to the sextet states gives a splitting of 223 cm^{-1}, it is reduced to 39 cm^{-1} with quartets and doublets and dynamical correlation (Table S7). Thus, a correct description requires numerous excited states and dynamical correlation, which is not feasible in the present case. As a compromise, the curve was fitted with a Van Vleck equation (eq S6) on the experimental magnetic susceptibility curve (Figure 6b and Note S3). The energy levels are now in better agreement with those published for $PuPd_2Sn$[42] and $PuCl_3$[43] (Figure 6d) also having an antiferromagnetic transition. More details about the fitting procedure, such as the nature of the states, as characterized by the g factors, can be found in the Supporting Information (Note S4, Figure S5, and Tables S8 and S9). Finally, the crystal field parameters (CFPs) and the crystal field strength were deduced (eq S7 and refs 44 and 45). The crystal field strength parameter S presented in Figure 6e translates, qualitatively, the degree of interaction between the f orbitals and the ligands. At the SF-CASSCF level, S is larger in Pu^{III} than in Sm^{III}, as a sign of the larger interaction of 5f than the semicore 4f orbitals with the ligand. However, with the fitted energies (Figure 6e), the spin−orbit coupling and the large J-

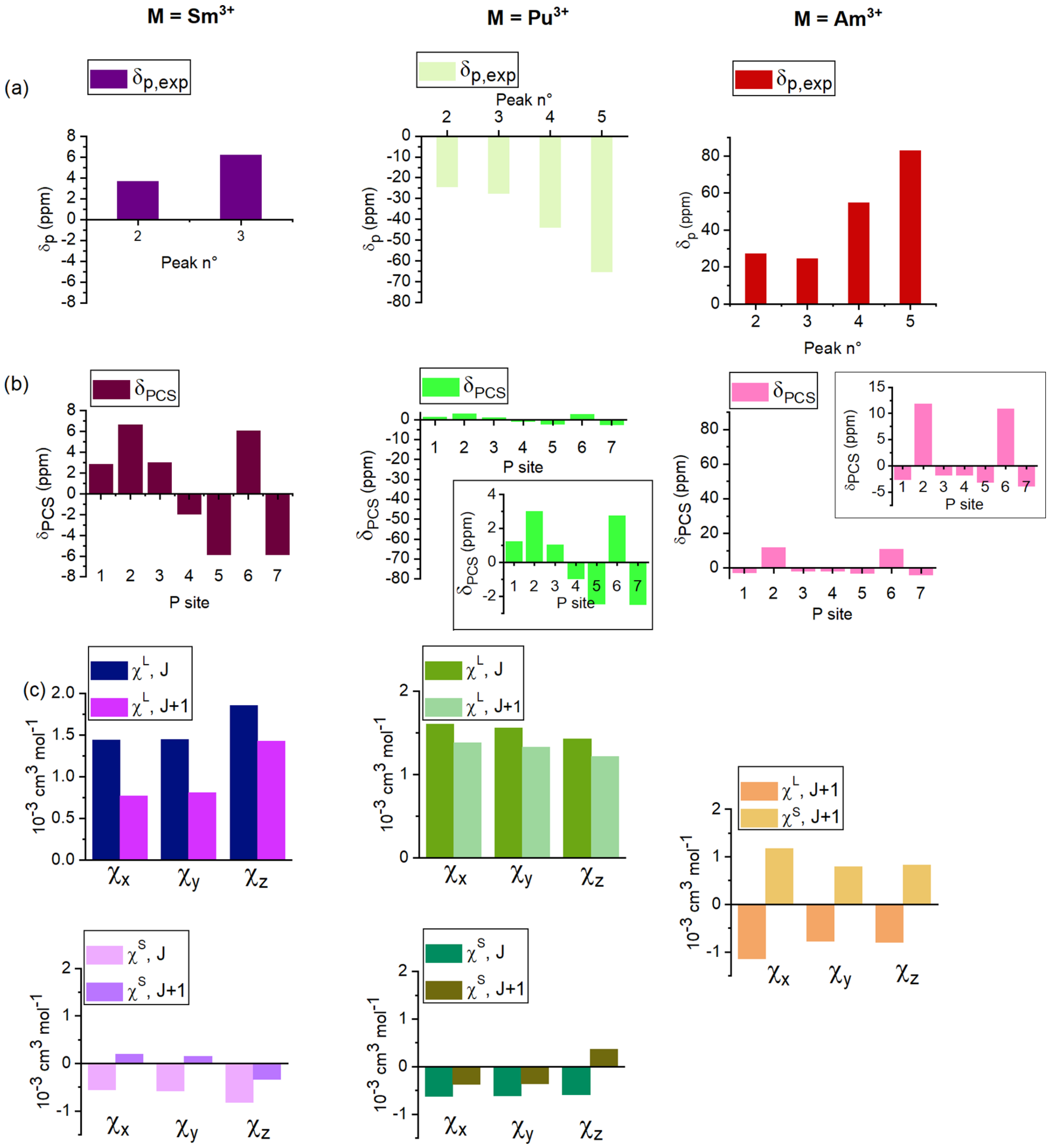

Figure 8. (a) Experimental paramagnetic shifts ($\delta_{p,exp}$) of $La_{0.9}M_{0.1}PO_4$, (b) calculated pseudocontact shifts (δ_{PCS}) (the insets show an enlargement of the δ_{PCS}), and (c) orbital (χ^L) and spin (χ^S) components of the magnetic susceptibility tensor (χ, in 10^{-3} cm^3 mol^{-1}).

mixing lead to the counterintuitive result that the effective crystal field splitting is smaller in the actinide analogue; this agrees with the $[PuCl_6]^{3-}$ complex results. The higher-order counterparts S^k show that, as it is usually the case,[45] the second order is dominant for the lanthanide complex, while the sixth order is important for the actinide one (Table S10).

3.5. Analysis of the Paramagnetic Shifts.

The pseudocontact shifts can be expressed in terms of the components of the magnetic susceptibility tensor and the geometrical factors of the NMR active nucleus (eq S1). The SO-CASSCF magnetic susceptibility tensors are given in Table 3. The three principal components, χ_x, χ_y, and χ_z, are similar, leading to a small anisotropy, which is due to the compactness of the coordination sphere—roughly spherical. The experimental paramagnetic shifts are shown in Figure 8a. As a consequence of the small anisotropy of the χ tensor, independently of the magnetic cation, the pseudocontact shift values range between ±10 ppm (Figure 8b and Table S11) and are slightly larger for the Sm^{III} and Am^{III}—with their larger values for χ_{iso} (Table 3). For the $La_{1-x}Sm_xPO_4$, the experimental paramagnetic shifts are of the same order of magnitude as the calculated pseudocontact shifts, while for the two actinide compounds, the $\delta_{p,exp}$ values are much larger (Figure 8). We can deduce that the Fermi contact contribution is, at most, of the same order of magnitude for $La_{1-x}Sm_xPO_4$ but dominant for both $La_{1-x}Pu_xPO_4$ and $La_{1-x}Am_xPO_4$.

The δ_{FCS} contribution, as expressed in eqs S2−S5 and refs 46 and 47, depends on the spin contribution to the magnetic susceptibility χ^S from the paramagnetic center and, on the spin density at the NMR active nucleus $K\rho^S(r_K)$. A full theoretical determination of δ_{FCS} was, unfortunately, not possible due to the difficulty in computing the term $K\rho^S(r_K)$. It is worth mentioning the successful work done in calculating the FCS using a multiconfigurational RASSCF method in refs 37 and 46, but it

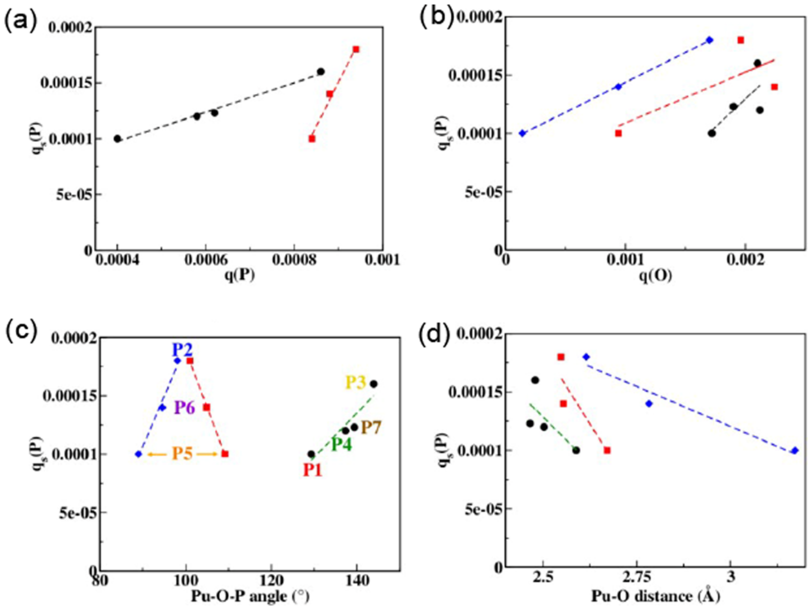

Figure 9. CASSCF calculations of Mulliken spin density in the s-orbitals of the P atoms (q_s(P)) against the Mulliken spin density on P (q(P)) and bridging O atoms (q(O)), Pu−O−P angles, and Pu−O distances for Pu^{III}. Black: monodentate phosphates; red and blue: bidentate phosphates, with smaller and larger angles, respectively. Dashed lines represent linear regressions.

was not applicable to the present cluster. Furthermore, as we cannot experimentally differentiate the P(OLa)$_6$(OM)$_1$ species, the indirect approach of determining the FCS values using $\delta_{FCS} = \delta_{p,exp} - \delta_{PCS}$ (assuming $\delta_{p,theo} = \delta_{p,exp}$) was also not possible. Therefore, we discuss qualitatively δ_{PCS} with the spin (χ^S)—and orbit (χ^L)—contribution to the magnetic susceptibility tensor. Table 3 can be understood as follows. The splitting of the ground state J = 5/2 manifold is smaller in Pu^{III} (90 cm^{-1}) than in Sm^{III} (240 cm^{-1}), allowing the three Kramers doublets to be populated at room temperature (Table S9). In the ground state J = 5/2 space, for the Sm^{III} and Pu^{III} complexes, the orbit contribution is large and positive, while the spin contribution is negative. For Am^{III}, in the ground state J = 1 space, the orbit contribution is this time negative and the spin contribution is positive. These opposite signs between χ^L and χ^S agree with the sign reversal stated by the third Hund's rule. For Sm^{III} and Pu^{III}, the effect of the second J-manifold (J = 7/2) has also to be considered (Table S6). For Pu^{III}, due to the larger spin−orbit coupling, the effect of the 7/2 manifold is reduced compared to Sm^{III}, which lies higher in energy (2500 vs 1000 cm^{-1}). As the effect of the second J-manifold is large for Sm^{III}, this reduces the orbit contribution and reverses the sign of the spin contribution[48] as previously stated by Bleaney.[36] For Pu^{III}, on the contrary, while both orbit and spin contributions decrease, there is this time no sign reversal. Thus, for the Pu^{III} complex, spin and orbit are opposite in sign, leading to a smaller χ_{iso} (0.58×10^{-3} cm^3 mol^{-1}) than for Sm^{III} (1.01×10^{-3} cm^3 mol^{-1}). For Am^{III}, the second J-manifold is too high in energy (∼4000 cm^{-1}) to have an impact. Thanks to this analysis, we show that χ^S is positive in Sm^{III} and Am^{III}, and negative in Pu^{III} similarly to the sign of the paramagnetic shift (Figure 8a,c). This implies that the spin density on all of the phosphorus nuclei is positive, in the three complexes.

We thus analyze qualitatively the delocalization of the spin density based on Mulliken charges (Table S12). The Mulliken charges in the s-orbitals of the phosphorus atom (q_s(P)) deduced from CASSCF calculations are different for the seven P atoms. While insignificant (0.0001−0.0003) in the Sm^{III} complex, it lies in the 0.0001−0.0018 range for the Pu^{III} and Am^{III} complexes (Figure 9 and Table S12), as expected from the larger covalent interaction for Sm^{III} and equivalent for Pu^{III} and Am^{III}. All of the P atoms are chemically equivalent in the center of a phosphate group, thus the delocalization of the spin density from the paramagnetic center to the phosphate depends on the bonding scheme. The most shifted peaks are expected to correspond to P atoms possessing the largest spin density at the nucleus. There are two types of bonding schemes of the phosphate ligands with a given Pu center: four of them bind through one oxygen atom and are monodentate, while the other three bind through two oxygen atoms and are bidentate (Figure 7). The Pu−O distances vary from 2.48 to 2.78 Å and the Pu−O−P angles from 94.6 to 144°. Figure 9 presents the dependence of the spin density in the s-orbital of the P atom (q_s(P)) against the Mulliken spin density on P (q(P)) and bridging O atoms (q(O)) and, selected crystalline parameters (Pu−O and Pu−O−P). We must underline that only the spin delocalization is described by our CASSCF calculations and, a larger active space should be considered for the description of the spin polarization. In Figure 9a, q_s(P) is compared to the whole Mulliken spin density on the same P atom q(P). As expected, they are proportional, but with different proportionality rates for monodentate and bidentate phosphates. While q(P) is larger for the bidentate, q_s(P) is not. The Pu−O distance is larger for the bidentate, and consequently, the Mulliken charge q(O) of the O bridging atom is smaller. q_s(P) seems to increase with q(O) (Figure 9b). Figure 9c shows that for the monodentate phosphates, the largest the Pu−O−P angle, the largest the q_s(P) value. For the bidentate, q_s(P) is the largest when the two angles are the same, corresponding to a symmetrical bonding by the two oxygen atoms. Finally, q_s(P) decreases with the Pu−O distance (Figure 9d). The analysis of the Mulliken charges supports the impact of the Fermi contact interaction on the different paramagnetic shifts, especially for the actinides, despite the unique crystallographic P site.

4. CONCLUSIONS

Using XRD, ^{31}P MAS-NMR, and magnetic susceptibility measurements, we fully characterized a series of crystalline monazites with a low metal content ($0 \leq x \leq 0.10$): lanthanide $La_{1-x}Sm_xPO_4$ and two actinides $La_{1-x}Pu_xPO_4$ and $La_{1-x}Am_xPO_4$. We successfully characterized the samples by XRD and extended the view of the local phosphorus environment in terms of $P(OLa)_m(OM)_{7-m}$ units thanks to NMR sensitivity to magnetism. We also confirmed that $La_{0.96}{}^{241}Am_{0.04}PO_4$ has a higher resistance to self-irradiation compared to $^{241}AmPO_4$. We delved deeper to understand the magnetism of each sample as it dominates the NMR spectra. We show that the magnetic susceptibility curves can be fitted with modified Curie−Weiss laws for $La_{1-x}Sm_xPO_4$ and $La_{1-x}Pu_xPO_4$ and, for $AmPO_4$ has a temperature-independent paramagnetism. An antiferromagnetic transition was properly identified at $T_N = 4$ K for $PuPO_4$. The determined effective moments point toward a localized nature of the 5f electrons. Strengthening by ab initio calculations, the magnetic susceptibility curves of $La_{1-x}Sm_xPO_4$ and $AmPO_4$ could be predicted. For $PuPO_4$, the curve was fitted with a Van Vleck fit. Indeed, we observed indirectly with a $[PuCl_6]^{3-}$ complex that, as the splitting of the ground state $J = 5/2$ was extremely sensitive to the quartets and to dynamical correlation, many quartet states will be necessary to properly predict the experimental curve. We then successfully extracted the energy levels and the crystal field strength parameters. Finally, we theoretically determined and discussed the paramagnetic shifts—compared to the experimental values—in terms of pseudocontact and Fermi contact shifts. We noticed that while the pseudocontact shifts—determined from the principal values χ_i of the magnetic susceptibility tensor and geometrical factors—were of the same order of magnitude as the paramagnetic shifts for $La_{1-x}Sm_xPO_4$, it was not the case for the actinide counterparts. We then qualitatively show, using the spin contribution of the magnetic susceptibility tensor χ^S, that the paramagnetic shift sign reversal—positive for $La_{1-x}Sm_xPO_4$ and $La_{1-x}Am_xPO_4$, negative for $La_{1-x}Pu_xPO_4$—was explained by the Fermi contact interaction. The further qualitative analysis of the delocalization of the spin density based on Mulliken charges strengthened this statement. This study is a pivotal stone for a better interpretation of solid-state paramagnetic NMR in actinides and opens door for further calculations of the hyperfine interaction. Our approach can be extended to numerous magnetic systems and nuclear waste matrices.

■ ASSOCIATED CONTENT

Supporting Information

The Supporting Information is available free of charge at https://pubs.acs.org/doi/10.1021/acs.jpcc.1c03957.

> X-ray diffraction (Note S1); relative intensities, experimental paramagnetic shifts, and definition of pseudocontact (PCS) and Fermi contact shifts (FCS) (Note S2); experimental magnetic susceptibilities (Note S3); energy levels and crystal field parameters (Note S4); and magnetic susceptibility tensors, pseudocontact shifts, and Mulliken charges (Note S5) (PDF)

■ AUTHOR INFORMATION

Corresponding Authors

Laura Martel − *Joint Research Centre (JRC), European Commission, 76125 Karlsruhe, Germany;* orcid.org/0000-0001-8554-2711; Email: lpm.martel@gmail.com

Jean-Christophe Griveau − *Joint Research Centre (JRC), European Commission, 76125 Karlsruhe, Germany;* Email: jean-christophe.griveau@ec.europa.eu

Authors

Md. Ashraful Islam − *Laboratoire de Chimie et Physique Quantiques, CNRS, Université Toulouse III, 31062 Toulouse, France*

Karin Popa − *Joint Research Centre (JRC), European Commission, 76125 Karlsruhe, Germany;* orcid.org/0000-0003-2759-6492

Jean-Francois Vigier − *Joint Research Centre (JRC), European Commission, 76125 Karlsruhe, Germany;* orcid.org/0000-0002-3640-1098

Eric Colineau − *Joint Research Centre (JRC), European Commission, 76125 Karlsruhe, Germany*

Hélène Bolvin − *Laboratoire de Chimie et Physique Quantiques, CNRS, Université Toulouse III, 31062 Toulouse, France;* orcid.org/0000-0002-6302-7820

Complete contact information is available at: https://pubs.acs.org/10.1021/acs.jpcc.1c03957

Author Contributions

K.P. and J.-F.V synthesized and characterized the samples by XRD. L.M. carried out the NMR experiments and their spectral analyses. J.-C.G., E.C., and L.M. prepared and conducted the magnetic susceptibility analyses. M.A.I., H.B., and L.M. conducted and contributed to the computational analyses. All of the authors made substantial contributions to the work reported in the manuscript.

Notes

The authors declare no competing financial interest.

■ ACKNOWLEDGMENTS

The authors are grateful to Dr. Joseph Somers for his fruitful scientific inputs and to Chris Selfslag and Daniel Bouexière for their help during the sample's preparation. H.B. and M.A.I. thanks the ANR under convention N-17- CE06-0010.

■ REFERENCES

(1) Guo, X.; Gin, S.; Lei, P.; Yao, T.; Liu, H.; Schreiber, D. K.; Ngo, D.; Viswanathan, G.; Li, T.; Kim, S. H.; et al. Self-accelerated corrosion of nuclear waste forms at material interfaces. *Nat. Mater.* **2020**, *19*, 310−316.

(2) Dacheux, N.; Clavier, N.; Podor, R. Monazite as a promising long-term radioactive waste matrix: Benefits of high-structural flexibility and chemical durability. *Am. Mineral.* **2013**, *98*, 833−847.

(3) Meldrum, A.; Boatner, L. A.; Weber, W. J.; Ewing, R. C. Radiation damage in zircon and monazite. *Geochim. Cosmochim. Acta* **1998**, *62*, 2509.

(4) Seydoux-Guillaume, A.-M.; Deschanels, X.; Baumier, C.; Neumeier, S.; Weber, W. J.; Peuget, S. Why natural monazite never becomes amorphous: Experimental evidence for alpha self-healing. *Am. Mineral.* **2018**, *103*, 824−827.

(5) Bregiroux, D.; Belin, R.; Valenza, P.; Audubert, F.; Bernache-Assollant, D. Plutonium and americium monazite materials: solid state synthesis and X-ray diffraction study. *J. Nucl. Mater.* **2007**, *366*, 52−57.

(6) Arinicheva, Y.; Popa, K.; Scheinost, A. C.; Rossberg, A.; Dieste-Blanco, O.; Raison, P.; Cambriani, A.; Somers, J.; Bosbach, D.; Neumeier, S. Structural investigations of $(La,Pu)PO_4$ monazite solid solutions: XRD and XAFS study. *J. Nucl. Mater.* **2017**, *493*, 404−411.

(7) Farnan, I.; Cho, H.; Weber, W. J. Quantification of actinide α-radiation damage in minerals and ceramics. *Nature* **2007**, *445*, 190−193.

(8) Palke, A. C.; Stebbins, J. F. Paramagnetic interactions in the ^{31}P NMR spectroscopy of rare earth element orthophosphate (REPO$_4$, monazite/xenotime) solid solutions. *Am. Mineral.* **2011**, *96*, 1343−1353.

(9) Maron, S.; Dantelle, G.; Gacoin, T.; Devreux, F. NMR and ESR relaxation in Nd- and Gd-doped LaPO$_4$: towards the accurate determination of the doping concentration. *Phys. Chem. Chem. Phys.* **2014**, *16*, 18788−18798.

(10) Martel, L.; Rakhmatullin, A.; Baldoví, J. J.; Perfetti, M.; Popa, K.; Deschamps, M.; Gouder, T.; Colineau, E.; Kovács, A.; Griveau, J.-C. Local structure and magnetism of La$_x$Eu$_{1-x}$PO$_4$ solid solutions. *Phys. Rev. B* **2019**, *100*, No. 054412.

(11) Pell, A. J.; Pintacuda, G.; Grey, C. P. Paramagnetic NMR in solution and in the solid-state. *Prog. Nucl. Magn. Reson. Spectrosc.* **2019**, *111*, 1−271.

(12) Panetti, G. B.; Sergentu, D.-C.; Gau, M. R.; Carroll, P. J.; Autschbach, J.; Walsh, P. J.; Schelter, E. J. Isolation and characterization of a covalent Ce(IV)-aryl complex with an anomalous ^{13}C chemical shift. *Nat. Commun.* **2021**, *12*, No. 1713.

(13) Geisler, T.; Popa, K.; Konings, R. J. M. Evidence for lattice strain and non-ideal behavior in the (La$_{1-x}$Eu$_x$)PO$_4$ solid solution from X-ray diffraction and vibrational spectroscopy. *Front. Earth Sci.* **2016**, *4*, No. 64.

(14) Martel, L.; Somers, J.; Berkmann, C.; Koepp, F.; Rothermel, A.; Pauvert, O.; Selfslag, C.; Farnan, I. A nuclear magnetic resonance spectrometer concept for hermetically sealed magic angle spinning investigations on highly toxic, radiotoxic, or air sensitive materials. *Rev. Sci. Instrum.* **2013**, *84*, No. 055112.

(15) Aquilante, F.; De Vico, L.; Ferré, N.; Ghigo, G.; Malmqvist, P.; Neogrády, P.; Bondo Pedersen, T.; Pitoňák, M.; Reiher, M.; Roos, B. O.; et al. R. MOLCAS 7: the next generation. *J. Comput. Chem.* **2010**, *31*, 224−247.

(16) Ni, Y.; Hughes, J. M.; Mariano, A. N. Crystal chemistry of the monazite and xenotime structures. *Am. Mineral.* **1995**, *80*, 21−26.

(17) Gagliardi, L.; Lindh, R.; Karlström, G. Local properties of quantum chemical systems: The Lo-Prop approach. *J. Chem. Phys.* **2004**, *121*, 4494−4500.

(18) Roos, B. O.; Lindh, R.; Malmqvist, P.; Veryazov, V.; Widmark, P. New Relativistic ANO Basis Sets for Transition Metal Atoms. *J. Phys. Chem. A* **2005**, *109*, 6575−6579.

(19) Hay, P. J.; Wadt, W. R. Ab initio effective core potentials for molecular calculations. Potentials for K to Au including the outermost core orbitals. *J. Chem. Phys.* **1985**, *82*, 299.

(20) Roos, B. O.; Taylor, P. R.; Siegbahn, P. E. M. A complete active space SCF method (CASSCF) using a density matrix formulated super-CI approach. *Chem. Phys.* **1980**, *48*, 157.

(21) Douglas, M.; Kroll, N. M. Quantum electrodynamical corrections to the fine structure of helium. *Ann. Phys.* **1974**, *82*, 89−155.

(22) Hess, B. A. Relativistic electronic-structure calculations employing a two-component no-pair formalism with external-field projection operators. *Phys. Rev. A* **1986**, *33*, 3742−3748.

(23) Malmqvist, P.-A.; Roos, B. O.; Schimmelpfennig, B. The restricted active space (RAS) state interaction approach with spin−orbit coupling. *Chem. Phys. Lett.* **2002**, *357*, 230.

(24) Iliaš, M.; Kello, V.; Visscher, L.; Schimmelpfennig, B. Inclusion of mean-field spin-orbit effects based on all-electron two-component spinors: Pilot calculations on atomic and molecular properties. *J. Chem. Phys.* **2001**, *115*, 9667−9674.

(25) Bolvin, H. An alternative approach to the g-matrix: theory and applications. *Chem. Phys. Chem.* **2006**, *7*, 1575.

(26) Jung, J.; Islam, M. A.; Pecoraro, V. L.; Mallah, T.; Berthon, C.; Bolvin, H. Derivation of Lanthanide Series Crystal Field Parameters From First Principles. *Chem. − Eur. J.* **2019**, *25*, 15112−15122.

(27) Ungur, L.; Chibotaru, L. F. Ab Initio crystal field for lanthanides. *Chem. − Eur. J.* **2017**, *23*, 3708−3718.

(28) Li, W.; Zhang, Q.; Joos, J. J.; Smet, P. F.; Schmedt auf der Günne, J. Blind spheres of paramagnetic dopants in solid state NMR. *Phys. Chem. Chem. Phys.* **2019**, *21*, 10185.

(29) Popa, K.; Vigier, J.-F.; Martel, L.; Manara, D.; Colle, J.-Y.; Dieste Blanco, O.; Wiss, T.; Freis, D.; Konings, R. J. M. Synthesis, characterization, and stability of americium phosphate, AmPO$_4$. *Inorg. Chem.* **2020**, *59*, 6595−6602.

(30) Weber, W. J.; Ewing, R. C.; Catlow, C. R. A.; Diaz de la Rubia, T.; Hobbs, L. W.; Kinoshita, C.; Matzke, H.; Motta, A. T.; Nastasi, M.; Salje, E. K. H.; et al. Radiation effects in crystalline ceramics for the immobilization of high-level nuclear waste and plutonium. *J. Mater. Res.* **1998**, *13*, 1434−1484.

(31) Deschanels, X.; Seydoux-Guillaume, A. M.; Magnin, V.; Mesbah, A.; Tribet, M.; Moloney, M. P.; Serruys, Y.; Peuget, S. Swelling induced by alpha decay in monazite and zirconolite ceramics: A XRD and TEM comparative study. *J. Nucl. Mater.* **2014**, *448*, 184−194.

(32) Bertini, I.; Luchinat, C. The hyperfine shift. *Coord. Chem. Rev.* **1996**, *150*, 29−75.

(33) Bertini, I.; Luchinat, C.; Parigi, G. Magnetic susceptibility in paramagnetic NMR. *Prog. Nucl. Magn. Reson. Spectrosc.* **2002**, *40*, 249−273.

(34) Soncini, A.; Van den Heuvel, W. Paramagnetic NMR chemical shift in a spin state subject to zero-field splitting. *J. Chem. Phys.* **2013**, *138*, No. 021103.

(35) Gendron, F.; Sharkas, K.; Autschbach, J. Calculating NMR chemical shifts for paramagnetic metal complexes from first-principles. *J. Phys. Chem. Lett.* **2015**, *6*, 2183−2188.

(36) Bleaney, B. Nuclear magnetic resonance shifts in solution due to lanthanide ions. *J. Magn. Reson. (1969)* **1972**, *8*, 91−100.

(37) Gendron, F.; Autschbach, J. Ligand NMR chemical shift calculations for paramagnetic metal complexes: 5f^1 vs 5f^2 actinides. *J. Chem. Theory Comput.* **2016**, *12*, 5309.

(38) Popa, K.; Colineau, E.; Wastin, F.; Konings, R. J. M. The low-temperature heat capacity of (Pu$_{0.1}$La$_{0.9}$)PO$_4$. *Solid State Commun.* **2007**, *144*, 74−77.

(39) Soderholm, L.; Edelstein, N.; Morss, L. R.; Shalimoff, G. V. The magnetic behavior of trivalent americium compounds. *J. Magn. Magn. Mater.* **1986**, *54−57*, 597−598.

(40) Frank, A. Temperature variation of the magnetic susceptibility, gyromagnetic ratio, and heat capacity in Sm^{3+} and Eu^{3+}. *Phys. Rev.* **1932**, *39*, 119−229.

(41) Gendron, F.; Autschbach, J. Puzzling lack of temperature dependence of the PuO$_2$ magnetic susceptibility explained according to ab initio wave function calculations. *J. Phys. Chem. Lett.* **2017**, *8*, 673−678.

(42) Gofryk, K.; Kaczorowski, D.; Griveau, J.-C.; Magnani, N.; Jardin, R.; Colineau, E.; Rebizant, J.; Wastin, F.; Caciuffo, R. Extensive studies of antiferromagnetic PuPd$_2$Sn. *Phys. Rev. B* **2008**, *77*, No. 014431.

(43) Jones, E. R., Jr.; Hendricks, M. E.; Stone, J. A.; Karraker, D. G. Magnetic properties of the trichlorides, tribromides, and triiodides of U(III), Np(III), and Pu(III). *J. Chem. Phys.* **1974**, *60*, 2088.

(44) Jung, J.; Islam, M. A.; Pecoraro, V. L.; Mallah, T.; Berthon, C.; Bolvin, H. Derivation of Lanthanide Series Crystal Field Parameters From First Principles. *Chem. − Eur. J.* **2019**, *25*, 15112−15122.

(45) Autillo, M.; Islam, M. A.; Jung, J.; Pilmé, J.; Galland, N.; Guerin, L.; Moisy, P.; Berthon, C.; Tamain, C.; Bolvin, H. Crystallographic structure and crystal field parameters in the $[\mathrm{An}^{\mathrm{IV}}(\mathrm{DPA})_3]^{2-}$ series, An = Th, U, Np, Pu. *Phys. Chem. Chem. Phys.* **2020**, *22*, 14293.

(46) Gendron, F.; Pritchard, B.; Bolvin, H.; Autschbach, J. Magnetic Resonance Properties of Actinyl Carbonate Complexes and Plutonyl(VI)-tris-nitrate. *Inorg. Chem.* **2014**, *53*, 8577−8592.

(47) Autillo, M.; Islam, M. A.; Héron, J.; Guérin, L.; Acher, E.; Tamain, C.; Illy, M.-C.; Moisy, P.; Colineau, E.; Griveau, J.-C.; et al. Temperature dependence of ^{1}H paramagnetic chemical shifts in actinide complexes, beyond Bleaney's theory. The $\mathrm{An}^{\mathrm{VI}}\mathrm{O}_2^{2+}$ dipicolinic acid complexes (An=Np, Pu) as an example. *Chem. − Eur. J.* **2021**, *27*, 7138−7153.

(48) Autillo, M.; Guerin, L.; Guillaumont, D.; Moisy, P.; Bolvin, H.; Berthon, C. Paramagnetism of aqueous actinide cations. Part II: Theoretical aspects and new measurements on An(IV). *Inorg. Chem.* **2016**, *55*, 12149−12157.

(49) Magnani, N.; Colineau, E.; Griveau, J.-C.; Apostolidis, C.; Walter, O.; Caciuffo, R. A plutonium-based single-molecule magnet. *Chem. Commun.* **2014**, *50*, 8171−8173.

(50) Gaggioli, C. A.; Gagliardi, L. Theoretical investigation of plutonium-based single-molecule magnets. *Inorg. Chem.* **2018**, *57*, 8098.